Computer Modeling in Engineering & Sciences
DOI:10.32604/cmes.2020.010719
Article

Numerical Simulation of Blood Flow in Aorta with Dilation: A Comparison between Laminar and LES Modeling Methods

Lijian Xu[1], Tianyang Yang[2], Lekang Yin[3], Ye Kong[2], Yuri Vassilevski[4,5] and Fuyou Liang[1,5,6,*]

[1]School of Naval Architecture, Ocean and Civil Engineering, Shanghai Jiao Tong University, Shanghai, 200240, China
[2]Shanghai Chest Hospital, Shanghai Jiao Tong University, Shanghai, 200030, China
[3]Zhongshan Hospital, Fudan University, Shanghai, 200032, China
[4]Marchuk Institute of Numerical Mathematics, Russian Academy of Sciences, Moscow, 119333, Russia
[5]Institute for Personalized Medicine, Sechenov University, Moscow, 119991, Russia
[6]Key Laboratory of Hydrodynamics (Ministry of Education), Shanghai Jiao Tong University, Shanghai, 200240, China
[*]Corresponding Author: Fuyou Liang. Email: fuyouliang@sjtu.edu.cn
Received: 23 March 2020; Accepted: 20 May 2020

Abstract: Computational modeling methods have been increasingly employed to quantify aortic hemodynamic parameters that are challenging to *in vivo* measurements but important for the diagnosis/treatment of aortic disease. Although the presence of turbulence-like behaviors of blood flow in normal or diseased aorta has long been confirmed, the majority of existing computational model studies adopted the laminar flow assumption (LFA) in the treatment of sub-grid flow variables. So far, it remains unclear whether LFA would significantly compromise the reliability of hemodynamic simulation. In the present study, we addressed the issue in the context of a specific aortopathy, namely aortic dilation, which is usually accompanied by disturbed flow patterns. Three patient-specific aortas with treated/untreated dilation of the ascending segment were investigated, and their geometrical models were reconstructed from computed tomography angiographic images, with the boundary conditions being prescribed based on flow velocity information measured *in vivo* with the phase contrast magnetic resonance imaging technique. For the modeling of blood flow, apart from the traditional LFA-based method in which sub-grid flow dynamics is ignored, the large eddy simulation (LES) method capable of incorporating the dissipative energy loss induced by turbulent eddies at the sub-grid level, was adopted and taken as a reference for examining the performance of the LFA-based method. Obtained results showed that the simulated large-scale flow patterns with the two methods had high similarity, both agreeing well with *in vivo* measurements, although locally large between-method discrepancies in computed hemodynamic quantities existed in regions with high intensity of flow turbulence. Quantitatively, a switch from the LES to the LFA-based modeling method led to mild (<6%) changes in computed space-averaged wall shear stress metrics (i.e., SA-TAWSS, SA-OSI) in the ascending aortic segment where intensive vortex evolution accompanied by high statistical Reynolds stress was observed. In addition, comparisons among the three aortas revealed that the treatment status of aortic dilation or the concomitant presence of aortic valve disease, despite its remarkable influence on flow patterns in the ascending aortic

segment, did not significantly affect the degrees of discrepancies between the two modeling methods in predicting SA-TAWSS and SA-OSI. These findings suggest that aortic dilation per se does not induce strong flow turbulence that substantially negates the validity of LFA-based modeling, especially in simulating macro-scale hemodynamic features.

Keywords: Blood flow; aortic dilation; computational modeling; turbulence; laminar flow assumption; large eddy simulation

1 Introduction

Aortic dilation is a common aortopathy that affects millions of people worldwide. Untreated aortic dilation may develop into aortic aneurysm, dissection or even lead to sudden rupture [1,2]. The natural history of an aorta with untreated dilation is complex and often exhibits highly patient-specific patterns [3,4]. In clinical practice, geometrical metrics are generally adopted as the standard indicator for risk stratification and decision making. On the other hand, hemodynamic parameters, which are closely associated with endothelial function and vascular pathophysiology [5,6], have been suggested to play potential roles in the pathogenesis and progression of aortic dilation [7]. In this sense, evaluating the characteristics of hemodynamics in dilated aortas may yield additional information of potential value for improving the diagnosis and treatment of aortic dilation.

Medical imaging techniques have been widely used to measure aortic geometry or hemodynamics in patients with aortic dilation, aortic valve anomalies or other aortopathies [3,8]. For instance, computed tomography angiography (CTA) scanning is routinely performed to determine the location and severity of aortic dilation [8]. It however lacks the ability to measure hemodynamic variables. This insufficiency can be remedied by phase contrast magnetic resonance imaging (PC-MRI), a technique capable of measuring flow velocities in any cross section of aorta [3]. Nevertheless, *in vivo* hemodynamic measurements generally lack a high level of temporal and spatial resolutions required for quantitative applications, especially the analysis of wall shear stress and its derivatives. In this context, computational modeling methods have been widely applied as a complement to *in vivo* measurements to gain high-precision hemodynamic information in aortas [9–12]. Despite the inherent advantages of computational modeling methods with respect to the precision and level of detail in hemodynamic quantification, the reliability of a computational model in reproducing *in vivo* hemodynamics is subjected to the influences of many factors involved in model setup [13]. For instance, it has been found that imposing idealized flow velocity profiles at the inlets of patient-specific aortic models causes significant deviations of model outputs from real *in vivo* hemodynamic conditions [14–16], which highlights the importance of patient-specifically prescribing model boundary conditions. Another important issue is relevant to the assumption on flow regimes (i.e., laminar, transitional, and turbulent flows) and the corresponding selection of fluid dynamics modeling method. Although laminar flow assumption is usually considered to be valid for blood flow in human arteries [17–21], and has been widely adopted in computational studies on aortic blood flow as well [14,16,22,23], *in vivo* studies have revealed the presence of flow turbulence in the ascending aortas of patients with aortic valve disease and highly unstable flow patterns in the aortas of healthy subjects [24,25]. In this sense, assuming blood flow to be strictly laminar might be problematic, especially in consideration of the increased flow complexity and disturbances associated with aortic dilation or concomitant aortic valve abnormalities [7,26,27]. To date, little is known about how the adoption of laminar flow assumption (LFA) in computational modeling of blood flow in dilated aortas would affect the outcome of numerical simulation.

To address the issue, we tested two fluid dynamics modeling methods on three aortas with treated or untreated dilation in the ascending aortic segment, namely the LFA-based method that has been widely

employed in previous studies, and the large eddy simulation (LES) method that has been proved capable of accounting for the evolution of a large range of turbulence eddies at a reasonable computational cost [28–31]. In order to compare the two modeling methods under physiologically realistic hemodynamic conditions, we reconstructed the geometrical model of each aorta from CTA images and prescribed the boundary conditions in a fully patient-specific way based on *in vivo* flow velocity information acquired by PC-MRI. The numerical results obtained by the two modeling methods were compared in terms of both large-scale flow patterns and local hemodynamic quantities. In addition, four-dimensional magnetic resonance imaging (4D-MRI) data of *in vivo* aortic blood flow were acquired and used as a reference for validating the results of numerical simulations.

2 Materials and Methods

2.1 Acquisition of Clinical Data

In this retrospective study, three patients diagnosed to have pathological dilation in the ascending aortic segment were enrolled, and, among them, two patients (i.e., patients #1 and #2) have not been treated, whereas one patient (patient #3) has undergone the David procedure to replace the severely dilated aortic segment with an artificial vessel. The ethics committee granted us exempt status for the use of the anonymized clinical data in this retrospective study. The main geometrical/hemodynamic parameters (derived from CTA or PC-MRI data) of the aortas and the pathophysiological states (determined by echocardiography) of the aortic valves are summarized in Tab. 1. From the data presented in Tab. 1, the three aortas differ evidently in terms of both geometry (e.g., maximum diameter) and hemodynamic state (e.g., mean and peak Reynolds numbers). CTA images of the aortas were acquired using a 64-channel multi-detector CT scanner (Philips Healthcare, The Netherlands) with standard techniques (slice thickness: 0.4 mm, in-plane spatial resolution: 512 × 512 pixels). Blood flow velocity quantities at the aortic inlet and in the cross-sections of main branch arteries were measured with a 3T MR scanner (Philips Healthcare, The Netherlands) operated in a PC-MRI sequence mode. Moreover, volumetric flow velocity information in the entire aorta was also measured using the flow-sensitive 4D-MRI technique to allow visualization of 3D flow patterns (the data were herein postprocessed with a validated software package (cmr42, Circle Cardiovascular Imaging Inc., Calgary, Alberta, Canada) [32]).

Table 1: Main geometrical and hemodynamic parameters of the aortas and pathophysiological states of the aortic valves in three patients

	Patient #1	Patient #2	Patient #3
Aortic disease	Mid-ascending aortic dilation	Mid-ascending aortic dilation	Mid-ascending aortic dilation
Status of treatment	Pre	Pre	Post
Morphotype of aortic valve	RL-BAV	TAV	TAV
Aortic valve stenosis	Severe	None	None
Aortic valve regurgitation	Moderate	Mild	Mild
Maximum diameter of aorta (mm)	45	52	30
Diameter of aortic inlet (mm)	38	38	28
Mean Re at aortic inlet	521	922	1688
Peak Re at aortic inlet	3257	4342	8000
Wo at aortic inlet	27.86	24.96	21.96

Abbreviations: BAV, bicuspid aortic valve; RL, right-left fusion; TAV, tricuspid aortic valve; Re, Reynolds number; Wo, Womersley number.

2.2 Model Reconstruction and Mesh Generation

The CTA images acquired from each patient were imported into Mimics 15.0 (Materialise, Belgium) to perform image segmentation and reconstruct a geometrical model for the aorta and its main branch arteries (see Fig. 1a). The reconstructed geometrical model was further read into ICEM 15.0 to generate a high-resolution mesh model with a hybrid meshing strategy, where the core region of fluid domain was divided by tetrahedral elements while the near-wall region by prism elements [12,33,34]. Allowing for the fact that a LES model generally requires higher mesh resolution than does a laminar model, we determined the minimum size of tetrahedral element and the thickness of prism-element layer based on

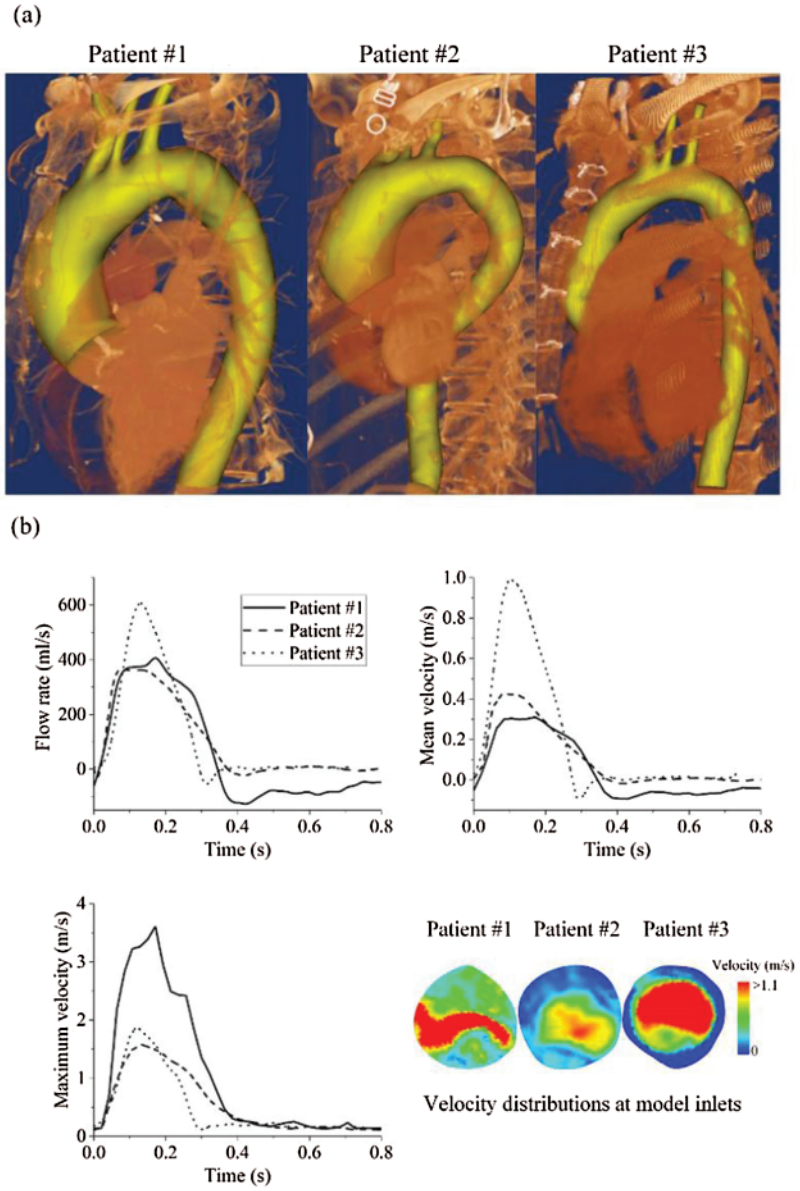

Figure 1: Geometrical models of aortas reconstructed from CTA images acquired from three patients with treated/untreated aortic dilation (a), and waveforms of volumetric flow rate, in-plane mean/maximum flow velocity as well as spatial distribution of flow velocity (at peak systole) at the model inlets derived from PC-MRI data (b)

the requirements of LES and performed grid independent analyses accordingly. With a minimum tetrahedral element size of 0.4 mm, our grid independent tests on the aortas of the three patients showed that further reducing the element sizes by 20% led to less than 0.5% changes in computed space-averaged wall shear stress and oscillatory shear index, indicating that the adopted mesh density is high enough to enable convergence of numerical solutions. As for the size of prism element, the thickness of the initial (i.e., closest to wall) layer was set to 30 μm, which was not only much smaller than the minimum size of interior tetrahedral element, but also small enough to ensure that the dimensionless wall distance y^+ is always less than 1.0 in all the near-wall regions. As a consequence, the mesh models of the three aortas contained 5592372, 7061034 and 6561363 elements, respectively.

2.3 Modeling of Blood Flow

Blood was assumed to be a homogeneous, incompressible fluid, with its density being set to 1060 kg/m^3. In consideration of the non-Newtonian rheology of blood, the shear-dependent variation in blood viscosity was represented with the Carreau model [35]. Blood flow was governed by the unsteady Navier-Stokes (N-S) equations. Although the N-S equations are, by definition, independent of flow regime, when they are discretized and numerically solved on a mesh model with finite element size, the ways of treating sub-grid flow variables would differ depending on the state of flow. If blood flow is in a strictly laminar state, flow variables can be assumed to distribute homogeneously within each individual element, in other words, sub-grid flow dynamics can be ignored; whereas if blood flow is turbulent, the presence of turbulent eddies smaller in scale than model element (i.e., sub-grid eddies) may induce considerable dissipative energy loss that should be incorporated into the solution of the large-scale (or grid-resolved) flow field. One approach to solving this problem is to keep refining the mesh model until the element size is smaller than the scales of all turbulent eddies, such as direct numerical simulation (DNS), which however often incurs unaffordable high computational cost, especially when dealing with models with complex geometry. A more practical way is to introduce sub-grid models capable of accounting for the contribution of sub-grid eddies whilst demanding much less computational effort compared with DNS [30,36].

In the present study, two fluid dynamics modeling methods were adopted and compared since flow regimes in the aortas are unknown. One was the laminar flow assumption (LFA)-based method that has been most commonly adopted by studies on arterial hemodynamics in the literature. Herein, the LFA-based method means that inhomogeneous flow dynamics and associated viscous energy loss at the sub-grid level are ignored when discretizing and solving the N-S equations on a mesh model, leaving the flow field to be represented by grid-resolved flow variables. The other one was the large eddy simulation (LES) method, which, by separating flow velocity (u_i) into a grid-resolved component ($\bar{u}_i$) and a sub-grid component (u_i'), enables the introduction of a sub-grid model to represent the energy loss associated with sub-grid eddies while solving the grid-resolved flow field [37,38], and hence can partly compensate for the deficiency of the LFA-based method. With the separation of flow velocity, the classical N-S equations were rewritten as

$$\frac{\partial \bar{u}_i}{\partial x_i} = 0, \tag{1}$$

$$\frac{\partial \bar{u}_i}{\partial t} + \bar{u}_j \frac{\partial \bar{u}_i}{\partial x_j} = -\frac{1}{\rho}\frac{\partial \bar{p}}{\partial x_i} + \frac{\partial}{\partial x_j}\left(\nu \frac{\partial \bar{u}_i}{\partial x_j}\right) + \frac{1}{\rho}\frac{\partial \tau_{ij}}{\partial x_j}, \tag{2}$$

where τ_{ij} is the sub-grid stress tensor that accounts for the dissipative effect of intra-element eddies.

In order to quantify the intensity of flow turbulence, we introduced the turbulent eddy viscosity (ν_t) and statistical Reynolds stress (R_{uu}) [39,40], which were defined respectively as

$$v_t = \left(\tau_{ij} - \frac{\delta_{ij}}{3}\tau_{kk}\right)/\left(-2\bar{S}_{ij}\right), \tag{3}$$

$$R_{uu} = \overline{u_i' u_i'}. \tag{4}$$

Here, $\boldsymbol{\delta_{ij}}$ is the Kronecker symbol and $\boldsymbol{\bar{S}_{ij}}$ the strain rate tensor of the grid-resolved velocity field ($\boldsymbol{i}, \boldsymbol{j}, \boldsymbol{k} = 1, 2, 3$). A more detailed description of the LES method has been reported in our previous study [12].

2.4 Boundary Conditions, Numerical Methods and Data Analysis

Time-varying flow velocity information extracted from patient-specific PC-MRI data was imposed at the inlet and outlets of each mesh model (see [12,41] for details on the methods of data extraction and image-to-model data projection). From Fig. 1b, flow conditions at the aortic inlet differ significantly among patients in terms of volumetric flow rate, mean flow velocity and in-plane velocity distribution, demonstrating the importance of patient-specifically prescribing boundary conditions. Fig. 2 shows the volumetric flow rate waveforms imposed at the inlet and outlets of the aortic model of a patient (i.e., patient #1). The magnitudes of the flow waveforms differ remarkably, reflecting the physiological flow division towards organs/tissues along the aorta. A free outflow boundary condition was prescribed at the outlet of the descending aorta to tolerate the phase and flow rate differences between aortic inflow and outflows through the branch arteries. In addition, all vascular walls were assumed to be rigid to which the non-slip boundary condition was imposed. For each model, the same set of boundary conditions was used despite the change in fluid dynamics modeling method.

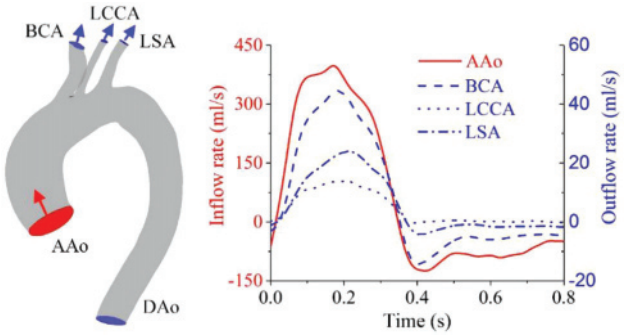

Figure 2: PC-MRI data-derived volumetric flow rate waveforms at the inlet (i.e., AAo) and outlets (i.e., BCA, LCCA, LSA, DAo) of the aorta model of patient #1. Abbreviations: AAo, ascending aorta; BCA, brachiocephalic artery; LCCA, left common carotid artery; LSA, left subclavian artery; DAo, descending aorta

Numerical simulations were implemented in a finite volume method-based commercial CFD package (ANSYS CFX 15). It is noted that for each aorta the governing equation systems corresponding to the LFA-based and LES modeling methods were solved on the same mesh model so as to minimize the influence of mesh-related numerical errors on between-method comparisons. Second-order upwind scheme and backward Euler scheme were adopted for spatial discretization of the convective term and time integration of the discretized equations, respectively. The numerical time step was fixed at 0.1 ms. At each time step, convergence of numerical solution was judged when the root mean-square residuals of the mass and momentum conservation equations all went below 10^{-5}. Each set of numerical simulation was continuously run for five cardiac cycles so that the solution could converge to a periodic one. Accordingly, numerical results obtained in the last (i.e., fifth) cardiac cycle were analyzed and reported.

All the numerical simulations were run on a Dell workstation (Precision T5610), taking about 48 and 85 hours on average for solving the laminar and LES models, respectively.

Analyses of numerical results were focused on flow velocity field, intensity of flow turbulence, as well as wall shear stress (WSS) and its derivatives that have been previously demonstrated to be associated with the pathogenesis of aortic disease, such as time-averaged wall shear stress (TAWSS) and oscillatory shear index (OSI) [3,42]. In order to gain an overall evaluation of WSS parameters in regions of interest (e.g., the ascending aortic segment), the model-predicted local TAWSS/OSI at each wall element was further spatially averaged (herein noted by SA-TAWSS/SA-OSI). Moreover, since we hypothesize that the LES method is more suitable than the LFA method for simulating aortic blood flow with potential turbulence, numerical results obtained with the LES method were set as the reference for evaluating the 'errors' of hemodynamic computation resulting from laminar flow assumption.

3 Results

3.1 Comparisons of Numerical Results with in vivo Measurements

Fig. 3 shows the model-simulated (with the LES and LFA methods) flow streamlines at peak systole (i.e., at the moment of peak flow velocity) in the aortas of three patients and their *in vivo* counterparts

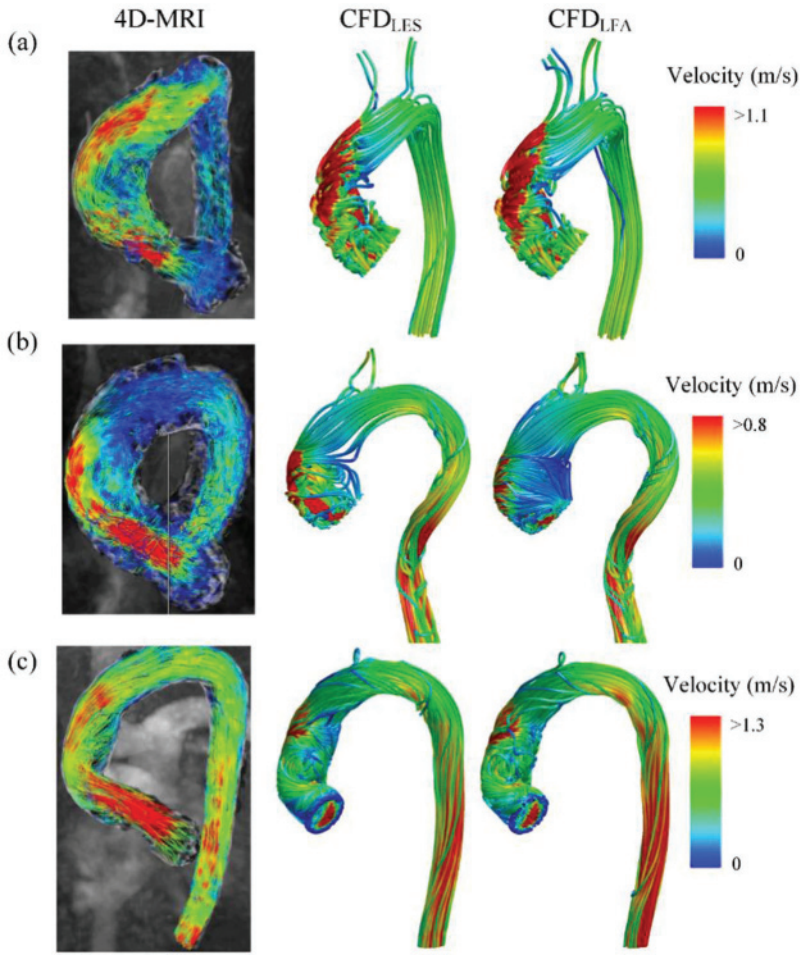

Figure 3: 4D-MRI-visualized flow streamlines (at the moment of peak systole) in the aortas of three patients (left panel) compared with those simulated by the CFD models established based on LES (middle panel) and LFA (right panel), respectively

obtained by 4D-MRI visualizations. The large-scale flow patterns (such as local concentration of high flow velocity, distribution of vortex) depicted by the numerical results and 4D-MRI data were in overall good agreement. Taking the aorta of patient #1 as an example, swirling flows directed from the aortic root toward the descending aorta accompanied by concentrated high flow velocities in the anterior region of the ascending aorta were detected by both the numerical simulation and *in vivo* measurement (see Fig. 3a). These results indicate that CFD models can reasonably reproduce *in vivo* hemodynamic characteristics if fully patient-specific geometrical model and boundary conditions are adopted. On the other hand, considerable discrepancies between model-simulated and measured flow fields were observed in some local regions, especially in the descending aortic segment. The discrepancies may be attributed to the introduction of assumptions/simplifications during model construction. For instance, the rigid-wall assumption rendered the models unable to represent the deformation of aortic wall and associated variation and phase change of flow waveform along the aorta that remarkably affect local flow patterns. In addition, the limited spatio-temporal resolutions of 4D-MRI measurement may also introduce errors into the visualized transient flow patterns, thereby contributing partly to the observed discrepancies between model simulations and *in vivo* measurements.

When the numerical results obtained by the LES and LFA methods were compared, the large-scale flow features were highly similar, although considerable discrepancies in flow velocity were observed in some local regions, such as in the ascending aortic segment where blood flow was highly disturbed.

3.2 Comparison of Transient Hemodynamic Quantities Computed with the LES and LFA Methods

Fig. 4 shows the comparison between the LES and LFA methods with respect to the simulated distributions of flow velocity and turbulent eddy viscosity in a longitudinal cutting plane of the ascending aorta of patient #1. Herein, the numerical results are visualized in form of snapshots at three typical time instants during a cardiac cycle (i.e., t_1 in the acceleration phase, t_2 at peak systole, and t_3 in the deceleration phase). The between-method differences were obtained by subtracting the results obtained by the LES method from those by the LFA method. The overall characteristics of flow velocity distribution predicted by the two modeling methods were in good agreement despite the presence of detectable local velocity differences that changed with time and became especially pronounced in the deceleration phase (t_3). The turbulent eddy viscosity (predicted by the LES model) tended to increase following the deceleration of blood flow, corresponding to the enlarged between-method differences in computed flow velocities at t_3.

Figs. 5 and 6 further show the comparisons of the simulated distributions of transient WSS in the three aortas with the two modeling methods. Similar to the observations for flow velocity, the most pronounced between-method differences appeared in the ascending aortic segment in the deceleration phase, although the degree of difference differed considerably among aortas, being largest for the aorta of patient #1 (see Fig. 5) while relatively small for the aortas of patients #2 and #3 (see Fig. 6).

3.3 Comparisons of WSS Metrics Computed with the LES and LFA Methods

Numerical results obtained by the LES and LFA modeling methods were further compared with respect to two WSS metrics, namely, TAWSS and OSI. From the contours of TAWSS presented in Fig. 7, the between-method difference in simulated TAWSS differed in terms of both magnitude and spatial distribution among aortas. For instance, large TAWSS differences were limited to the ascending aorta of patient #1, but distributed over the entire aorta of patient #3. Relatively, the magnitude of between-method difference was much smaller in the aorta of patient #2. These phenomena were also confirmed by comparing the values of TAWSS along a curve at the front wall of aorta. With regard to OSI, the between-method difference was comparable in magnitude among the three aortas (see Fig. 8). Basically,

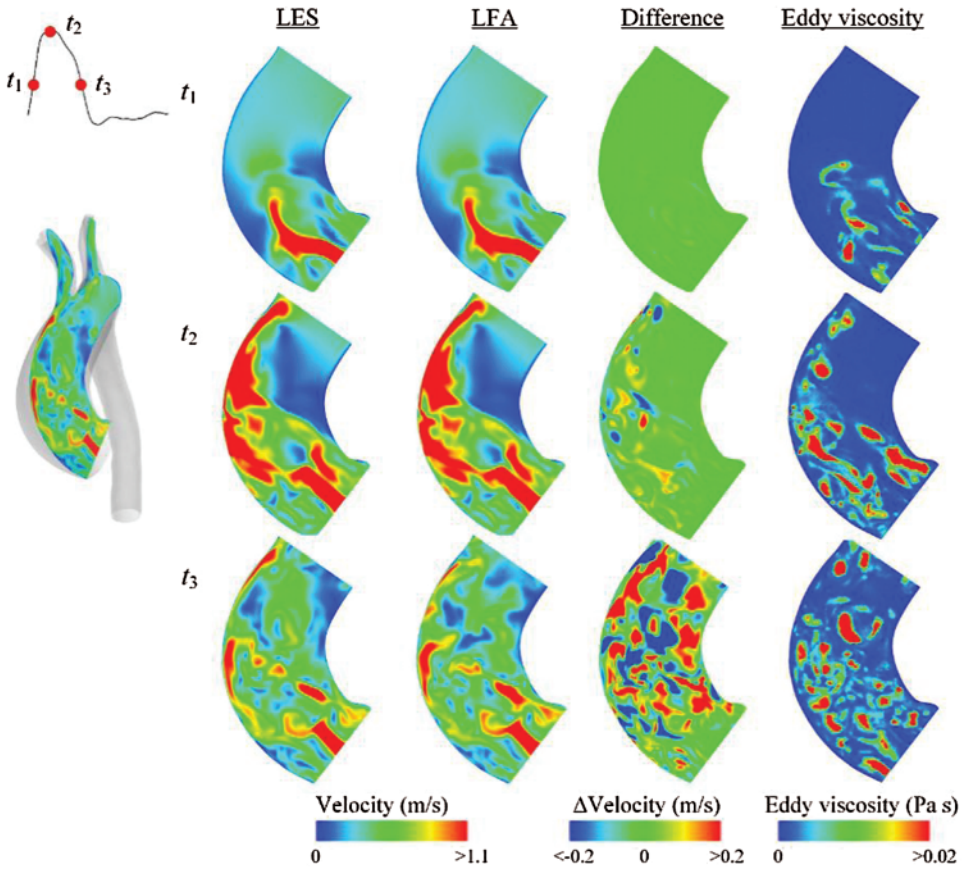

Figure 4: Comparisons of the simulated flow patterns (presented in form of filled velocity contours in a longitudinal cutting plane at three selected time instants (i.e., t_1, t_2 and t_3 in the acceleration phase, at peak systole, and in the deceleration phase, respectively) during a cardiac cycle) in the aorta of patient #1 with the LES and LFA methods. The visualized data of between-method difference have been calculated by subtracting the numerical results obtained by the LES method from those obtained by the LFA method. The color maps of eddy viscosity (shown in the rightmost panel) indicate the time-varying intensity and distribution of flow turbulence predicted by the LES model

large between-method differences appeared mainly in the ascending aortic segment for all the three aortas, as could also be observed from the plots of OSI along the front wall of aorta.

The space-averaged TAWSS and OSI in the ascending aorta of each patient (i.e., SA-TAWSS, SA-OSI) presented in Fig. 9 indicate that the choice of fluid dynamics modeling method had small influence (less than 6%) on both SA-TAWSS and SA-OSI, although the exact changes caused by the switch of the LES method to the LFA method differed among aortas.

To further explore mechanisms underlying the observed between-method differences in computed flow velocity and WSS, we further plot the time-averaged (over a cardiac cycle) vortex structures in form of iso-surface of Lambda 2 (at a level value of 0.05) colored by the statistical Reynolds stress in Fig. 10. Complex vortex structures accompanied by high statistical Reynolds stress were present mainly in the ascending aortic segment, which corresponds well with the overall larger between-method differences in computed hemodynamic quantities in this region than those in the descending aortic segment. However, the spatial

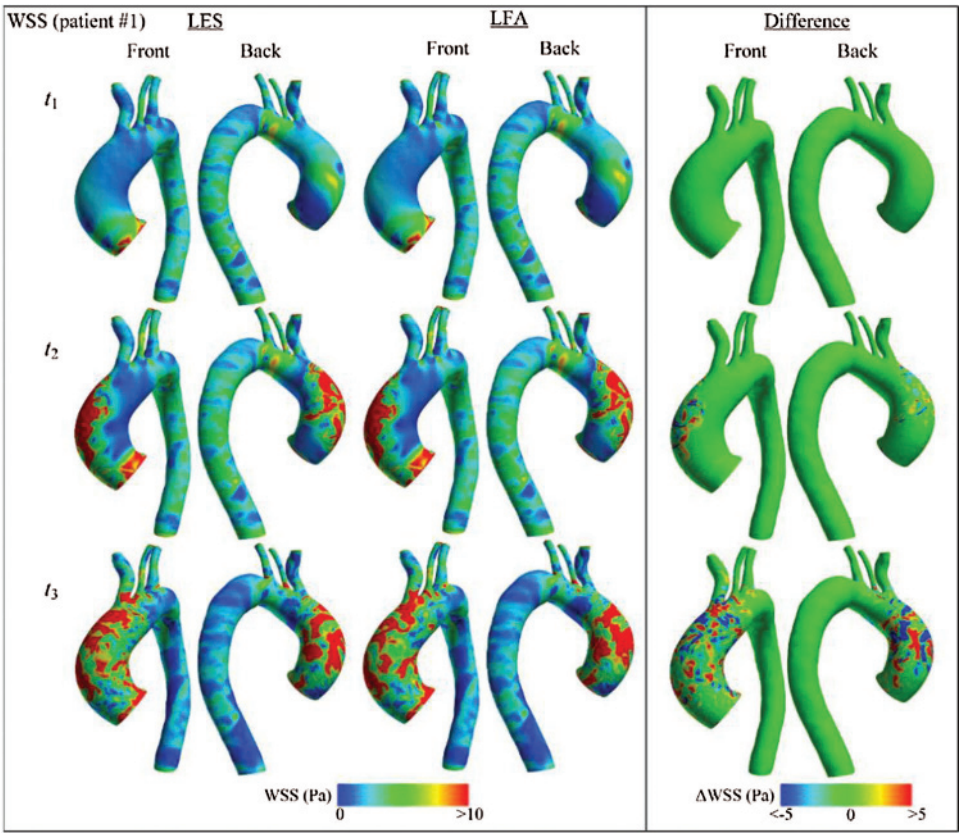

Figure 5: Comparisons of the LES and LFA methods with respect to the simulated distribution of transient WSS (at three time instants during a cardiac cycle as noted in Fig. 4) in the aorta of patient #1

distribution of strong vortex or high statistical Reynolds stress differed considerably among aortas, indicating the highly aorta-specific characteristics.

4 Discussion

The main purpose of the present study was to investigate how the selection of fluid dynamics modeling method would affect the outcome of numerical simulation of blood flow in aorta with untreated or treated dilation. The utilization of patient-specific aortic geometry (reconstructed from CTA images) and prescription of boundary conditions based strictly on *in vivo* measurements (by PC-MRI) enabled the resulting models to reasonably reproduce 4D-MRI-visualized *in vivo* flow patterns, thus yielding a physiologically realistic numerical platform for testing different fluid dynamics modeling methods. In addition, although the three patients enrolled in the present study all had aortic dilation, the differential combinations of treatment status of aortic dilation and aortic valve function made them representative of different patient cohorts. For instance, patient #1 had untreated aortic dilation combined with abnormal aortic valve function featured by a BAV morphotype and severe stenosis, whereas patient #2 only suffered from the pathological condition related to aortic dilation, and thus they can represent two typical cohorts of patients with aortic dilation but differential aortic valve functions. Patient #3, however, had a close to normal aortic valve function and aortic morphology after David procedure, and can represent patients without aortic dilation and aortic valve disease. The presence of strong swirling flow in the ascending aortic segment and elevated WSS at the anterior wall was predicted for both of the dilated aortas (of patients #1 and #2), although the degree of WSS elevation was higher and the wall area

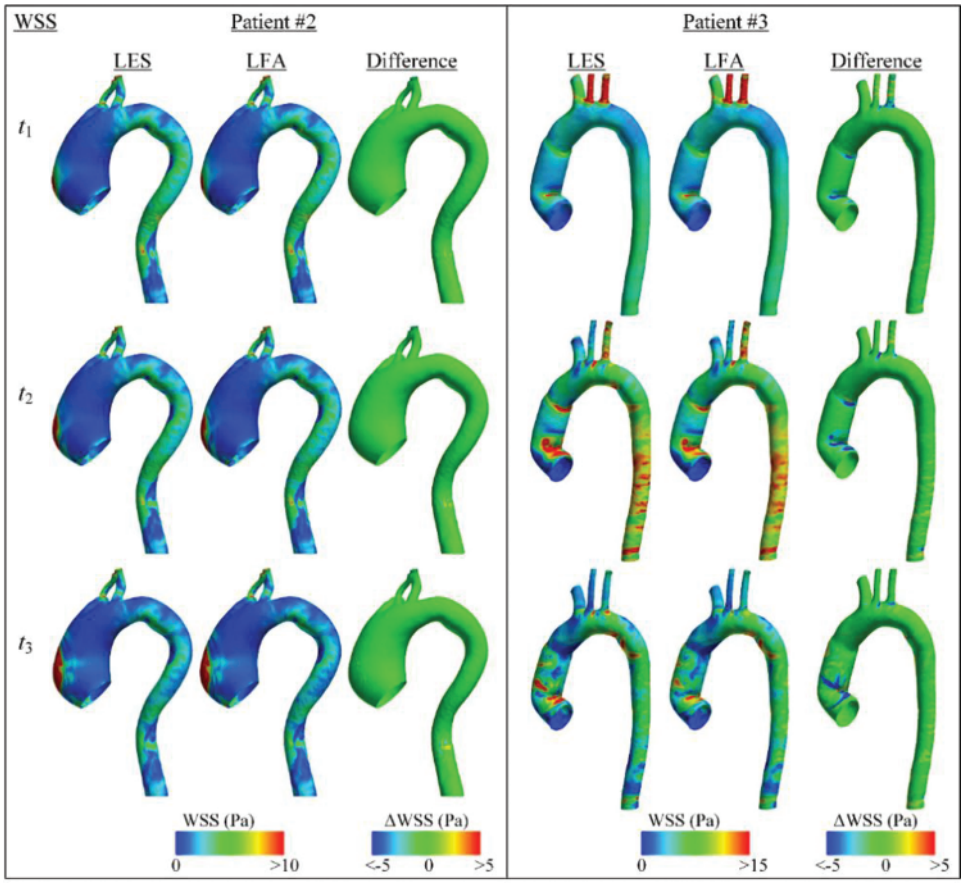

Figure 6: Comparisons of the LES and LFA methods with respect to the simulated distributions of transient WSS in the aortas of patient #2 and patient #3

exposed to high WSS was larger in the aorta of patient #1 (with stenosed RL-BAV) compared with those in the aorta of patient #2 (with non-stenotic TAV), which is consistent with previous findings regarding the respective/combined effects of aortic dilation and BAV on the characteristics of aortic blood flow and WSS distribution [3,4,7,9,43–45]. In contrast, there was no evident swirling flow and focal elevation of WSS in the ascending aortic segment of the aorta of patient #3, which indicated the remarkable differences between flow patterns in normal and dilated aortas. Main findings with respect to the effects of fluid dynamics modeling methods on the outcome of hemodynamic simulation include: 1) large-scale hemodynamic features (e.g., vortex structure, WSS distribution) simulated with the LES method and LFA method were highly similar, with the between-method differences in computed SA-TAWSS and SA-OSI in the ascending aortic segment being less than 6%; 2) relatively large between-method differences in hemodynamic prediction were more likely to appear in the ascending aortic segment and became more pronounced in the deceleration phase; and 3) between-method differences in computed hemodynamic quantities varied considerably among aortas in terms of magnitude and spatial distribution.

The first finding indicates that adopting the laminar flow assumption in the modeling of aortic blood flow would not cause the simulated large-scale flow patterns to deviate significantly from those obtained with the LES method that is expected to better account for potential flow turbulence, although differences between hemodynamic quantities computed with the two methods were detectable, especially in regions where the intensity of turbulence was high (indicated by the high value of turbulent eddy viscosity or statistical

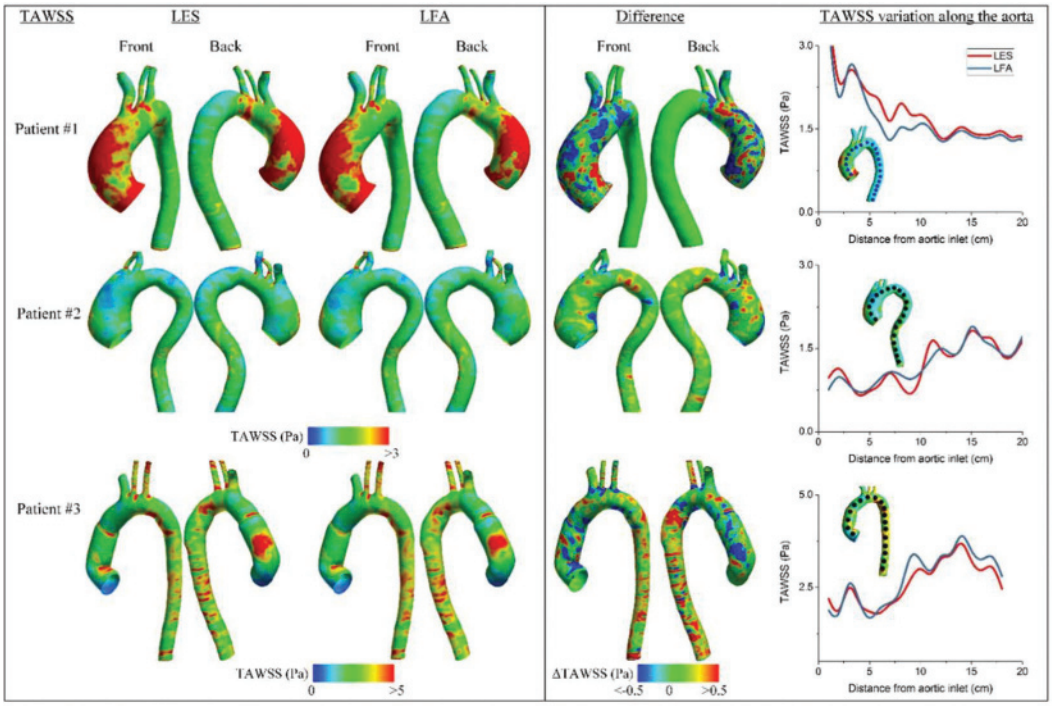

Figure 7: Comparisons of the LES and LFA methods with respect to the simulated distributions of TAWSS in the aortas of three patients. TAWSSs at selected locations (indicated by the filled circles) along the front wall of each aorta are plotted in the rightmost panel to give a clearer quantitative comparison

Reynolds stress). In another word, the occurrence of flow turbulence in the aortas did not significantly alter the large-scale flow patterns. In comparison with the selection of fluid dynamics modeling method, the prescription of boundary conditions for an aortic model may have greater influence on the outcome of numerical simulation. For instance, it has been found that imposing an idealized flow velocity profile instead of the realistic one (measured by PC-MRI) at the aortic inlet may cause the predicted TAWSS in the ascending aorta to change by up to 80% [14–16], a value much larger than the predicted changes (<6%) in TAWSS due to the switch of the LES method to the LFA method. In addition, given the higher computational cost of turbulent modeling method (e.g., the computation time required by the LES method was about twice of that by the LFA method), the LFA method may be more practical in consideration of the balance between cost and benefit. In this sense, whether flow turbulence should be well treated is a less important issue in patient-specific modeling of aortic blood flow, at least for normal or dilated aortas. However, under some specific pathological conditions, such as in the presence of severe aortic stenosis, the occurrence of strong flow turbulence in the post-stenosis region may largely compromise the validity of laminar flow assumption [28,31], and in such cases the use of turbulence modeling methods would be more worthy of recommendation.

The second and third findings point to the considerable dependence of between-method differences in numerical results on aorta-specific hemodynamic conditions. Theoretically, flow patterns in an aorta are co-determined by multiple factors, such as the morphology of aorta, upstream/downstream flow conditions, and flow pulsation. The three aortas investigated in the present study differ significantly not only in morphology but also in flow conditions at the aortic inlet, which can account for the marked inter-aorta differences in simulated flow patterns. For each individual aorta, the ascending aortic segment is usually more susceptible than the descending segment to flow disturbance due to the effects of complex inflow from

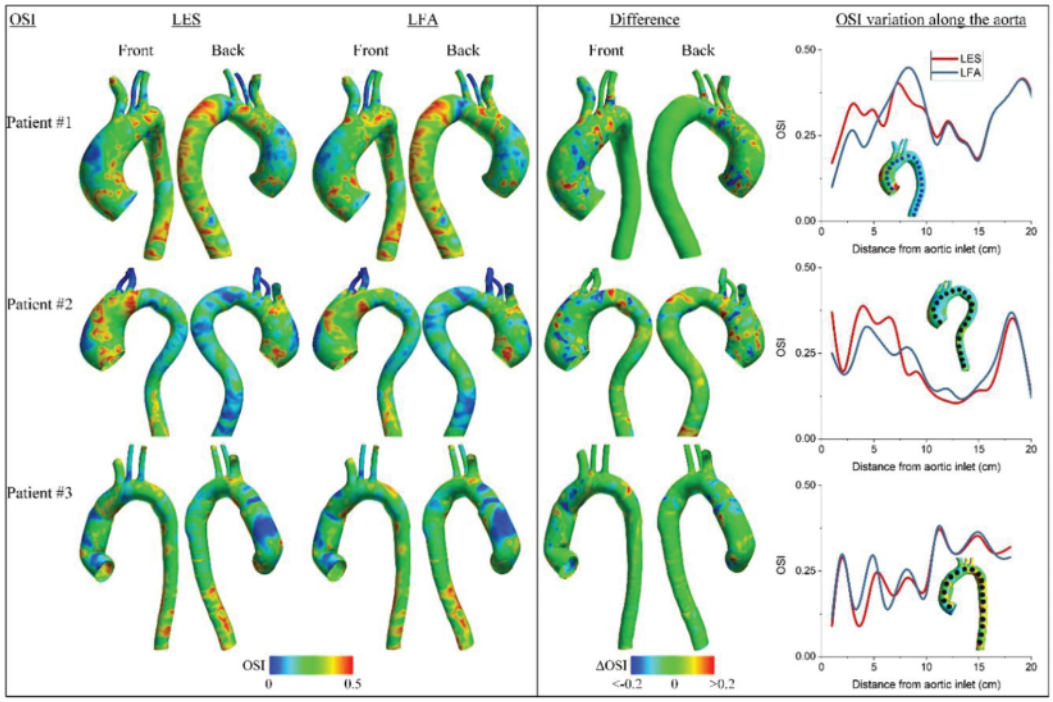

Figure 8: Comparisons of the LES and LFA methods with respect to the simulated distributions of OSI in the aortas of three patients. OSIs at selected locations (indicated by the filled circles) along the front wall of each aorta are plotted in the rightmost panel to give a clearer quantitative comparison

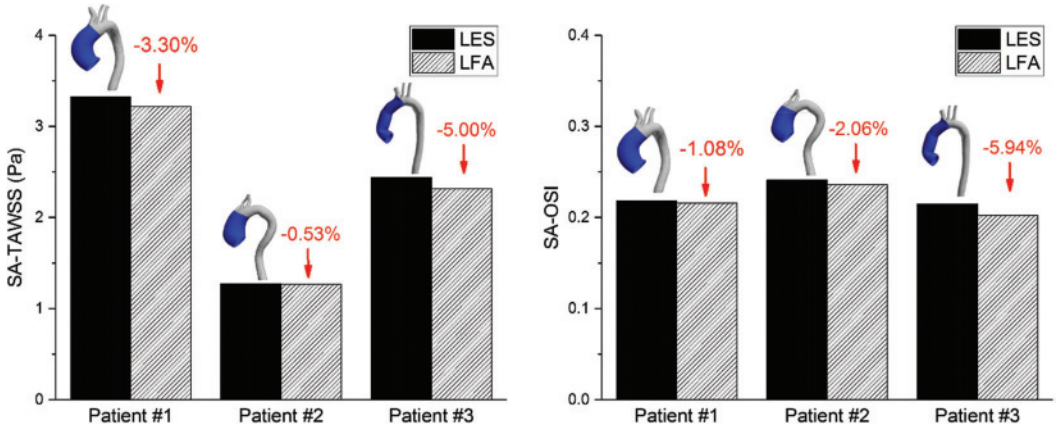

Figure 9: Comparisons of the LES and LFA methods with respect to the simulated space-averaged TAWSS (SA-TAWSS) (a) and OSI (SA-OSI) (b) in the ascending aortic segments (highlighted by blue in the geometrical models) of the three aortas. The numbers shown in each sub-figure indicate the percent changes of the LFA method-obtained results relative to those obtained by the LES method

the heart and aortic valve and the high vascular tortuosity [16,22,23,46], which may explain the finding of the present study that high intensity of flow turbulence and intensive vortex evolution appeared mainly in the ascending aortic segment. On the other hand, the highly patient-specific aortic morphology and aortic valve function caused the intensity of flow turbulence in the ascending aortic segment to differ significantly among the three patients, consequently leading to differential degrees of between-method

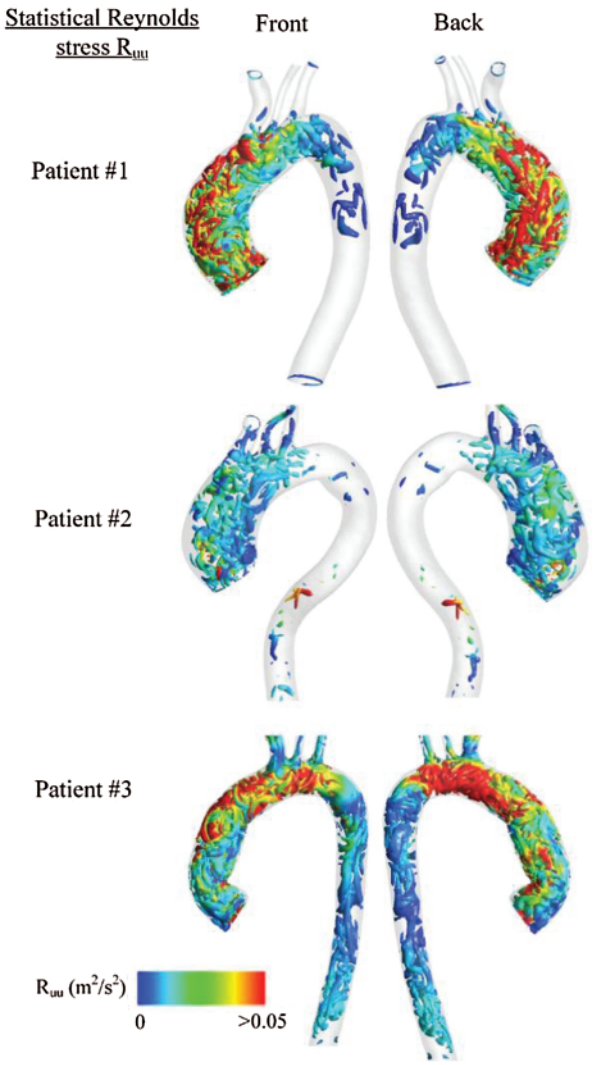

Figure 10: Vortex structures represented by iso-surfaces of time-averaged (over a cardiac cycle) Lambda-2 at a level value of 0.05 colored by the statistical Reynolds stress in the aortas of three patients

differences in computed hemodynamic quantities. It has been reported that the morphotype of aortic valve has remarkable influence on blood flow patterns in the ascending aorta, and that BAV represents a typical valve morphotype associated with aortic flow abnormalities [9,43–45,47,48]. Similarly, our study showed that the stenosed BAV in patient #1 caused the distribution of high-speed flows at the aortic inlet to be more concentrated and asymmetric (see Fig. 1b), which may have considerably increased the disturbance of flow to promote laminar to turbulent transition in the ascending aorta (indicated by high turbulent eddy viscosity and statistical Reynolds stress), consequently leading to larger deviations of hemodynamic quantities computed with the LFA method from those with the LES method in patient #1 than in patient #2 whose aortic valve is of a normal tricuspid morphotype and free of stenosis. Interestingly, despite the close to normal aortic morphology and aortic valve function in patient #3, the between-method differences in SA-TAWSS and SA-OSI in the ascending aortic segment were largest among the three patients (see Fig. 9). A major causative factor for this phenomenon is the higher Reynolds number in the aorta of patient #3 than in the aortas of patients #1 and #2 (see Tab. 1). These findings suggest that a

variety of patient-specific factors are involved in determining the intensity and distribution of flow turbulence in the aorta, and that aortic dilation per se does not significantly elevate the level of flow turbulence to necessitate the adoption of turbulence modeling method, although coexistence of aortic valve disease may augment flow turbulence according to our study and previous relevant studies [25,44].

The present study is subject to several limitations related to the choices of aorta for investigation and modeling methods for test. First, we investigated the sensitivities of computed hemodynamic quantities to the selection of fluid dynamic modeling method in only three aortas with untreated/treated dilation. The small number of aortas might render the findings rather aorta-specific than universally applicable to aortas with different types and severities of dilation and/or aortic valve abnormality. In particular, it remains unclear whether the findings would be applicable to aortas suffering from other aortopathies (e.g., aortic stenosis, aneurysm or dissection) that affect the characteristics of aortic flow in different ways [28,31,49,50]. Second, the LES method, despite the well proved performance in simulating arterial blood flow with potential turbulence, cannot resolve all scales of turbulent eddies due to the limited spatio-temporal resolution [28,30,31]. At this point, direct numerical simulation may be a more advanced approach, but it is immensely expensive in terms of computational cost [51,52] and could hardly be applied to deal with blood flows in anatomically realistic aortic models, such as those addressed in the present study. Third, aortic walls were assumed to be rigid in the study, which rendered the models unable to account for the effects of aortic wall deformation on intra-aortic flow patterns. Physiologically, aortic walls deform dynamically over a cardiac cycle in response to the pulsation of blood pressure [53,54]. Previous studies on aortic blood flow have demonstrated that ignoring the deformation of aortic wall leads to considerable overestimate of WSS [55–56], but its effects on flow turbulence remain unclear and would deserve further investigations.

5 Conclusions

Blood flows in three patient-specific aortas with untreated/treated dilation were numerically studied with the LFA-based and LES modeling methods, respectively. It was found that the simulated flow patterns with the two modeling methods were of high similarity despite the widely-distributed local discrepancies in computed hemodynamic quantities. Quantitatively, the predicted space-averaged WSS metrics in the ascending aortic segment with the two methods differed by less than 6% in all the three aortas. These findings suggest that for aortas with dilation, modeling blood flow based on laminar flow assumption is, in general, acceptable if large-scale flow features are of major interest.

Funding Statement: The study was supported by the National Natural Science Foundation of China (Grant nos. 11972231, 11832003, 81611530715), the China Postdoctoral Science Foundation (Grant no. 2018M640385), and the SJTU Medical-Engineering Cross-cutting Research Project (Grant no. YG2017MS45).

Conflicts of Interest: The authors declare that they have no conflicts of interest to report regarding the present study.

References

1. Benedetti, N., Hope, M. D. (2015). Prevalence and significance of incidentally noted dilation of the ascending aorta on routine chest computed tomography in older patients. *Journal of Computer Assisted Tomography, 39(1),* 109–111. DOI 10.1097/RCT.0000000000000167.
2. Verma, S., Siu, S. C. (2014). Aortic dilatation in patients with bicuspid aortic valve. *New England Journal of Medicine, 370(20),* 1920–1929. DOI 10.1056/NEJMra1207059.
3. Barker, A. J., Lanning, C., Shandas, R. (2010). Quantification of hemodynamic wall shear stress in patients with bicuspid aortic valve using phase-contrast MRI. *Annals of Biomedical Engineering, 38(3),* 788–800. DOI 10.1007/s10439-009-9854-3.

4. Pasta, S., Rinaudo, A., Luca, A., Pilato, M., Scardulla, C. et al. (2013). Difference in hemodynamic and wall stress of ascending thoracic aortic aneurysms with bicuspid and tricuspid aortic valve. *Journal of Biomechanics, 46(10),* 1729–1738. DOI 10.1016/j.jbiomech.2013.03.029.
5. Balistreri, C. R., Crapanzano, F., Schirone, L., Allegra, A., Pisano, C. et al. (2018). Deregulation of Notch1 pathway and circulating endothelial progenitor cell (EPC) number in patients with bicuspid aortic valve with and without ascending aorta aneurysm. *Scientific Reports, 8(1),* 1–10. DOI 10.1038/s41598-018-32170-2.
6. Tzemos, N., Lyseggen, E., Silversides, C., Jamorski, M., Tong, J. H. et al. (2010). Endothelial function, carotid-femoral stiffness, and plasma matrix metalloproteinase-2 in men with bicuspid aortic valve and dilated aorta. *Journal of the American College of Cardiology, 55(7),* 660–668. DOI 10.1016/j.jacc.2009.08.080.
7. Bissell, M. M., Hess, A. T., Biasiolli, L., Glaze, S. J., Loudon, M. et al. (2013). Aortic dilation in bicuspid aortic valve disease: flow pattern is a major contributor and differs with valve fusion type. *Circulation: Cardiovascular Imaging, 6(4),* 499–507. DOI 10.1161/CIRCIMAGING.113.000528.
8. Leipsic, J., Gurvitch, R., LaBounty, T. M., Min, J. K., Wood, D. et al. (2011). Multidetector computed tomography in transcatheter aortic valve implantation. *JACC: Cardiovascular Imaging, 4(4),* 416–429. DOI 10.1016/j.jcmg.2011.01.014.
9. Cao, K., Atkins, S. K., McNally, A., Liu, J., Sucosky, P. (2017). Simulations of morphotype-dependent hemodynamics in non-dilated bicuspid aortic valve aortas. *Journal of Biomechanics, 50,* 63–70. DOI 10.1016/j.jbiomech.2016.11.024.
10. Kousera, C. A., Wood, N. B., Seed, W. A., Torii, R., O'regan, D. et al. (2013). A numerical study of aortic flow stability and comparison with *in vivo* flow measurements. *Journal of Biomechanical Engineering, 135(1),* 179. DOI 10.1115/1.4023132.
11. Pirola, S., Guo, B., Menichini, C., Saitta, S., Fu, W. et al. (2019). 4-D flow MRI-based computational analysis of blood flow in patient-specific aortic dissection. *IEEE Transactions on Biomedical Engineering, 66(12),* 3411–3419. DOI 10.1109/TBME.2019.2904885.
12. Xu, L., Yin, L., Liu, Y., Liang, F. (2019). A computational study on the influence of aortic valve disease on hemodynamics in dilated aorta. *Mathematical Biosciences and Engineering: MBE, 17(1),* 606–626. DOI 10.3934/mbe.2020031.
13. Liang, F., Oshima, M., Huang, H., Liu, H., Takagi, S. (2015). Numerical study of cerebroarterial hemodynamic changes following carotid artery operation: a comparison between multiscale modeling and stand-alone three-dimensional modeling. *Journal of Biomechanical Engineering, 137(10),* 1849. DOI 10.1115/1.4031457.
14. Gallo, D., De Santis, G., Negri, F., Tresoldi, D., Ponzini, R. et al. (2012). On the use of *in vivo* measured flow rates as boundary conditions for image-based hemodynamic models of the human aorta: implications for indicators of abnormal flow. *Annals of Biomedical Engineering, 40(3),* 729–741. DOI 10.1007/s10439-011-0431-1.
15. Goubergrits, L., Mevert, R., Yevtushenko, P., Schaller, J., Kertzscher, U. et al. (2013). The impact of MRI-based inflow for the hemodynamic evaluation of aortic coarctation. *Annals of Biomedical Engineering, 41(12),* 2575–2587. DOI 10.1007/s10439-013-0879-2.
16. Morbiducci, U., Ponzini, R., Gallo, D., Bignardi, C., Rizzo, G. (2013). Inflow boundary conditions for image-based computational hemodynamics: impact of idealized *vs.* measured velocity profiles in the human aorta. *Journal of Biomechanics, 46(1),* 102–109. DOI 10.1016/j.jbiomech.2012.10.012.
17. Cebral, J. R., Mut, F., Weir, J., Putman, C. (2011). Quantitative characterization of the hemodynamic environment in ruptured and unruptured brain aneurysms. *American Journal of Neuroradiology, 32(1),* 145–151. DOI 10.3174/ajnr.A2419.
18. Li, X., Liu, X., Li, X., Xu, L., Chen, X. et al. (2019). Tortuosity of the superficial femoral artery and its influence on blood flow patterns and risk of atherosclerosis. *Biomechanics and Modeling in Mechanobiology, 18(4),* 883–896. DOI 10.1007/s10237-019-01118-4.
19. Xiang, J., Natarajan, S. K., Tremmel, M., Ma, D., Mocco, J. et al. (2011). Hemodynamic-morphologic discriminants for intracranial aneurysm rupture. *Stroke, 42(1),* 144–152. DOI 10.1161/STROKEAHA.110.592923.
20. Xu, L., Liang, F., Gu, L., Liu, H. (2018). Flow instability detected in ruptured *vs.* unruptured cerebral aneurysms at the internal carotid artery. *Journal of Biomechanics, 72,* 187–199. DOI 10.1016/j.jbiomech.2018.03.014.

21. Zhang, Z. Q., Xu, L. J., Liu, R., Liu, X. S., Zhao, B. et al. (2019). Importance of incorporating systemic cerebroarterial hemodynamics into computational modeling of blood flow in intracranial aneurysm. *Journal of Hydrodynamics, 44(11),* 3018. DOI 10.1007/s42241-019-0038-9.

22. Pirola, S., Cheng, Z., Jarral, O. A., O'Regan, D. P., Pepper, J. R. et al. (2017). On the choice of outlet boundary conditions for patient-specific analysis of aortic flow using computational fluid dynamics. *Journal of Biomechanics, 60,* 15–21. DOI 10.1016/j.jbiomech.2017.06.005.

23. Singh, S. D., Xu, X. Y., Wood, N. B., Pepper, J. R., Izgi, C. et al. (2016). Aortic flow patterns before and after personalised external aortic root support implantation in Marfan patients. *Journal of Biomechanics, 49(1),* 100–111. DOI 10.1016/j.jbiomech.2015.11.040.

24. Stalder, A. F., Frydrychowicz, A., Russe, M. F., Korvink, J. G., Hennig, J. et al. (2011). Assessment of flow instabilities in the healthy aorta using flow-sensitive MRI. *Journal of Magnetic Resonance Imaging, 33(4),* 839–846. DOI 10.1002/jmri.22512.

25. Stein, P. D., Sabbah, H. N. (1976). Turbulent blood flow in the ascending aorta of humans with normal and diseased aortic valves. *Circulation Research, 39(1),* 58–65. DOI 10.1161/01.RES.39.1.58.

26. Cheng, Z., Kidher, E., Jarral, O. A., O'Regan, D. P., Wood, N. B. et al. (2016). Assessment of hemodynamic conditions in the aorta following root replacement with composite valve-conduit graft. *Annals of Biomedical Engineering, 44(5),* 1392–1404. DOI 10.1007/s10439-015-1453-x.

27. Numata, S., Itatani, K., Kanda, K., Doi, K., Yamazaki, S. et al. (2016): Blood flow analysis of the aortic arch using computational fluid dynamics. *European Journal of Cardio-Thoracic Surgery, 49, (6),* 1578–1585. DOI 10.1093/ejcts/ezv459.

28. Andersson, M., Ebbers, T., Karlsson, M. (2019). Characterization and estimation of turbulence-related wall shear stress in patient-specific pulsatile blood flow. *Journal of Biomechanics, 85,* 108–117. DOI 10.1016/j.jbiomech.2019.01.016.

29. Johari, N. H., Wood, N. B., Cheng, Z., Torii, R., Oishi, M. et al. (2019): Disturbed flow in a stenosed carotid artery bifurcation: comparison of RANS-based transitional model and LES with experimental measurements. *International Journal of Applied Mechanics, 11, (04),* 1950032. DOI 10.1142/S1758825119500327.

30. Li, C., Jiang, J., Dong, H., Zhao, K. (2017). Computational modeling and validation of human nasal airflow under various breathing conditions. *Journal of Biomechanics, 64,* 59–68. DOI 10.1016/j.jbiomech.2017.08.031.

31. Molla, M. M., Paul, M. C. (2012). LES of non-Newtonian physiological blood flow in a model of arterial stenosis. *Medical Engineering & Physics, 34(8),* 1079–1087. DOI 10.1016/j.medengphy.2011.11.013.

32. Trauzeddel, R. F., Löbe, U., Barker, A. J., Gelsinger, C., Butter, C. et al. (2016). Blood flow characteristics in the ascending aorta after TAVI compared to surgical aortic valve replacement. *The International Journal of Cardiovascular Imaging, 32(3),* 461–467. DOI 10.1007/s10554-015-0792-x.

33. Liang, F., Liu, X., Yamaguchi, R., Liu, H. (2016). Sensitivity of flow patterns in aneurysms on the anterior communicating artery to anatomic variations of the cerebral arterial network. *Journal of Biomechanics, 49(15),* 3731–3740. DOI 10.1016/j.jbiomech.2016.09.031.

34. Zhou, X., Yin, L., Xu, L., Liang, F. (2020). Non-periodicity of blood flow and its influence on wall shear stress in the carotid artery bifurcation: an *in vivo* measurement-based computational study. *Journal of Biomechanics, 101,* 109617. DOI 10.1016/j.jbiomech.2020.109617.

35. Liu, X., Fan, Y., Deng, X., Zhan, F. (2011). Effect of non-Newtonian and pulsatile blood flow on mass transport in the human aorta. *Journal of Biomechanics, 44(6),* 1123–1131. DOI 10.1016/j.jbiomech.2011.01.024.

36. Tan, F. P. P., Wood, N. B., Tabor, G., Xu, X. Y. (2011). Comparison of LES of steady transitional flow in an idealized stenosed axisymmetric artery model with a RANS transitional model. *Journal of Biomechanical Engineering, 133(5),* 401. DOI 10.1115/1.4003782.

37. Collins, R. E. (1976). *Flow of fluids through porous materials*. Tulsa, USA: Petroleum Publishing Co.

38. Hinze, J. O. (1975). *Turbulence*. New York, USA: McGraw-Hill Publishing Co.

39. Farrell, B. F., Gayme, D. F., Ioannou, P. J. (2017). A statistical state dynamics approach to wall turbulence. *Philosophical Transactions of the Royal Society A: Mathematical, Physical and Engineering Sciences, 375 (2089),* 20160081. DOI 10.1098/rsta.2016.0081.

40. Nicoud, F., Ducros, F. (1999). Subgrid-scale stress modelling based on the square of the velocity gradient tensor. *Flow, Turbulence and Combustion, 62(3),* 183–200. DOI 10.1023/A:1009995426001.
41. Gomez, A., Marčan, M., Arthurs, C. J., Wright, R., Youssefi, P. et al. (2018). Optimal B-spline mapping of flow imaging data for imposing patient-specific velocity profiles in computational hemodynamics. *IEEE Transactions on Biomedical Engineering, 66(7),* 1872–1883. DOI 10.1109/TBME.2018.2880606.
42. Barker, A. J., Markl, M., Bürk, J., Lorenz, R., Bock, J. et al. (2012). Bicuspid aortic valve is associated with altered wall shear stress in the ascending aorta. *Circulation: Cardiovascular Imaging, 5(4),* 457–466. DOI 10.1161/CIRCIMAGING.112.973370.
43. Liu, J., Shar, J. A., Sucosky, P. (2018). Wall shear stress directional abnormalities in BAV aortas: toward a new hemodynamic predictor of aortopathy? *Frontiers in Physiology, 9,* 1209. DOI 10.3389/fphys.2018.00993.
44. McNally, A., Madan, A., Sucosky, P. (2017). Morphotype-dependent flow characteristics in bicuspid aortic valve ascending aortas: a benchtop particle image velocimetry study. *Frontiers in Physiology, 8,* 44. DOI 10.3389/fphys.2017.00044.
45. Oliveira, D., Rosa, S. A., Tiago, J., Ferreira, R. C., Agapito, A. F. et al. (2019). Bicuspid aortic valve aortopathies: an hemodynamics characterization in dilated aortas. *Computer Methods in Biomechanics and Biomedical Engineering, 22(8),* 815–826. DOI 10.1080/10255842.2019.1597860.
46. Alastruey, J., Siggers, J. H., Peiffer, V., Doorly, D. J., Sherwin, S. J. (2012). Reducing the data: analysis of the role of vascular geometry on blood flow patterns in curved vessels. *Physics of Fluids, 24(3),* 031902. DOI 10.1063/1.3694526.
47. Barker, A. J., van Ooij, P., Bandi, K., Garcia, J., Albaghdadi, M. et al. (2014). Viscous energy loss in the presence of abnormal aortic flow. *Magnetic Resonance in Medicine, 72(3),* 620–628. DOI 10.1002/mrm.24962.
48. Barker, A. J., Markl, M., Fedak, P. W. (2018). Assessing wall stresses in bicuspid aortic valve-associated aortopathy: Forecasting the perfect storm? *The Journal of Thoracic and Cardiovascular Surgery, 156(2),* 471–472. DOI 10.1016/j.jtcvs.2018.03.092.
49. Menichini, C., Cheng, Z., Gibbs, R. G., Xu, X. Y. (2018). A computational model for false lumen thrombosis in type B aortic dissection following thoracic endovascular repair. *Journal of Biomechanics, 66,* 36–43. DOI 10.1016/j.jbiomech.2017.10.029.
50. Romarowski, R. M., Faggiano, E., Conti, M., Reali, A., Morganti, S. et al. (2019). A novel computational framework to predict patient-specific hemodynamics after TEVAR: integration of structural and fluid-dynamics analysis by image elaboration. *Computers & Fluids, 179,* 806–819. DOI 10.1016/j.compfluid.2018.06.002.
51. Mittal, R., Simmons, S. P., Najjar, F. (2003). Numerical study of pulsatile flow in a constricted channel. *Journal of Fluid Mechanics, 485,* 337–378. DOI 10.1017/S002211200300449X.
52. Zhu, C., Seo, J. H., Mittal, R. (2018). Computational modelling and analysis of haemodynamics in a simple model of aortic stenosis. *Journal of Fluid Mechanics, 851,* 23–49. DOI 10.1017/jfm.2018.463.
53. Dobroserdova, T., Liang, F., Panasenko, G., Vassilevski, Y. (2019). Multiscale models of blood flow in the compliant aortic bifurcation. *Applied Mathematics Letters, 93,* 98–104. DOI 10.1016/j.aml.2019.01.037.
54. Liang, F., Takagi, S., Himeno, R., Liu, H. (2009). Multi-scale modeling of the human cardiovascular system with applications to aortic valvular and arterial stenoses. *Medical & Biological Engineering & Computing, 47(7),* 743–755. DOI 10.1007/s11517-009-0449-9.
55. Alimohammadi, M., Sherwood, J. M., Karimpour, M., Agu, O., Balabani, S. et al. (2015). Aortic dissection simulation models for clinical support: fluid-structure interaction *vs.* rigid wall models. *BioMedical Engineering OnLine, 14(1),* 1661. DOI 10.1186/s12938-015-0032-6.
56. Bonfanti, M., Balabani, S., Alimohammadi, M., Agu, O., Homer-Vanniasinkam, S. et al. (2018). A simplified method to account for wall motion in patient-specific blood flow simulations of aortic dissection: comparison with fluid-structure interaction. *Medical Engineering & Physics, 58,* 72–79. DOI 10.1016/j.medengphy.2018.04.014.